Nanosecond time scale transient optoplasmonic detection of single proteins

Baaske Martin, D.; Asgari Nasrin; Punj Deep; Orrit Michel

OPTICS

Nanosecond time scale transient optoplasmonic detection of single proteins

Martin D. Baaske, Nasrin Asgari, Deep Punj, Michel Orrit*

Optical detection of individual proteins with high bandwidth holds great promise for understanding important biological processes on the nanoscale and for high-throughput fingerprinting applications. As fluorescent labels impose restrictions on detection bandwidth and require time-intensive and invasive processes, label-free optical techniques are highly desirable. Here, we read out changes in the resonantly scattered field of individual gold nanorods interferometrically and use photothermal spectroscopy to optimize the experiment's parameters. This interferometric plasmonic scattering enables the observation of single proteins as they traverse plasmonic near fields of gold nanorods with unprecedented temporal resolution in the nanosecond-to-microsecond range.

INTRODUCTION

Almost all biological processes involve enzymatic action. Enzyme function is often accompanied by conformational changes that can occur on microsecond time scales—substantially faster than the enzyme's turnover rate (*1*). Essential elementary steps in protein folding and unfolding may occur on microsecond (*2*, *3*) and even nanosecond (*4*) time scales. As probing assays for such fast dynamics often rely on single-molecule fluorescence, they require the analysis of thousands of single molecules (*5*). The need for such massive numbers arises directly from the limited bandwidth of fluorescence detection and from the restrictions in observation time imposed by dye blinking and bleaching. The biological processes discussed above have one thing in common: They involve motion. Therefore, label-free methods with high bandwidth able to resolve such motion are highly desirable. Here, we propose observations of the diffusive motion of whole proteins as a starting point for the development of such methods. In addition, the observation of protein motion by itself holds great promise for high-throughput fingerprinting applications. Translational and rotational motion carries information about such protein properties as size and shape. Protein charge and dipole moment can be probed by electrophoresis and dielectrophoresis if the sample is subjected to external electric fields. Optoplasmonic methods are promising candidates as high-bandwidth sensing platforms, as single-molecule sensitivity has been demonstrated repeatedly (*6*–*14*). State-of-the-art optoplasmonic methods typically exhibit time resolutions on the order of milliseconds and rely on analyte immobilization to facilitate detection. The need for analyte immobilization is a direct consequence of the minuscule dimensions of plasmonic near fields typically providing sub-attoliter–sized detection volumes that, in turn, demand sub-microsecond temporal resolution for the direct detection of proteins in motion. Here, we show that such temporal resolution can indeed be achieved. We demonstrate the observation of single proteins as small as hemoglobin [Hem; molecular weight (MW): 64 kDa] as they traverse plasmonic near fields of gold nanorods (NRs) and interact with their surface, all while maintaining signal-to-noise ratios (SNRs) larger than 5 and an unprecedented temporal resolution well below microseconds. This method enables the label-free observation of single-molecule dynamics on previously inaccessible time scales.

Huygens-Kamerlingh Onnes Laboratory, Leiden University, Postbus 9504, 2300 RA Leiden, Netherlands.
*Corresponding author. Email: orrit@physics.leidenuniv.nl

RESULTS

Sensor principle

To achieve such resolution, we have improved the confocal system we had previously used to detect single metal nanoparticles in Brownian motion (*15*). Our system recognizes perturbations of dielectric environment inside a plasmonic NR's near field caused by nano-objects such as nanoparticles, micelles, or proteins. Such perturbations alter the NR's polarizability and shift the frequency ν_{NR} of its localized surface plasmon resonance (LSPR), resulting in a change of the scattered field's amplitude E_s and its phase difference ϕ with respect to the incident field. The quantity we detect is the intensity $I_{det} \propto |E_r|^2 + |E_s|^2 + 2|E_r||E_s| \cos(\phi + \gamma)$, which is a result of the interference between scattered E_s and reflected E_r fields with phase difference $\phi + \gamma$, where γ denotes the Gouy phase. More specifically, we are interested in its changes

$$\Delta I_{det} \propto [\,|E_s| + |E_r| \cos(\phi + \gamma)\,]\Delta|E_s| - |E_r||E_s| \sin(\phi + \gamma)\,\Delta\phi \quad (1)$$

Here, the left-hand $\Delta|E_s|$ term, which denotes the change of the scattered field, is the quantity typically detected by interference scattering methods (*16*, *17*), which aim to recognize the transition between the absence and the presence of a, not necessarily resonantly, scattering nano-object. In contrast, our method aims to detect changes in the cross section and resonance frequency of an otherwise static resonant scatterer. In this case, the $\Delta\phi$ term gains importance for field-strength ratios $R_F = |E_s/E_r| < 1$. Established interference scattering–based methods use selective reduction of the reflected beam's intensity by spatial filtering (*18*, *19*) to tune R_F and optimize contrast. We, however, can make use of the NR's scattering anisotropy and tune R_F via choice of incident and analyzed linear polarizations (*15*). Disregarding NR dimensions and fixing the NR's position in the center of the probe beam, we have access to four adjustable parameters that influence the sensitivity of a single NR: Incident and analyzed polarizations tune R_F, the probe laser's frequency tunes R_F and ϕ, and the Gouy-phase γ can be adjusted via the distance Δz between NR and the objective's focal plane. Other parameters that affect SNRs are probe power, NR dimensions, LSPR linewidth, and hardware specifications like the noise-equivalent

power (NEP) and excess noise factor of the detector. The optimization of parameters based on the observation of signal amplitudes resulting from random perturbations caused by diffusing analytes (*15*) is too slow and too indirect. We are thus looking for a means that enables us to directly probe our system's response to changes in an NR's polarizability that (i) is independent of analyte properties, (ii) does not involve chemical modification of the NR, and (iii) can be easily controlled and implemented. We found that photothermal spectroscopy is a convenient method that fulfills all of these requirements.

Photothermal calibration

Photothermal spectroscopy detects minute changes in refractive index that follow the absorption of light by an analyte and the consequent dissipation of heat into the surrounding medium (*20*–*23*). Here, we use the sensor NR as absorber. Absorption of the intensity-modulated heating beam (wavelength: 532 nm) alters the polarizability of the NR via the thermo-refractive effect and gives rise to changes in the probe beam's intensity at the heating beam's modulation frequency ν_H. This process is similar to analyte-induced changes of NR polarizability and is a result of the same contrast mechanism, namely, the change of effective dielectric contrast between the NR and the surrounding medium. In consequence, the photothermal response is well suited as a proportional probe for relative changes in detected intensity $\Delta I_{Det}/I_{Det}$. Specifically, we determine the relative photothermal amplitude $A_{PT} = \frac{A(\nu_H)}{A(\nu_P)}$, where $A(\nu)$ denotes the root mean square (rms) amplitude at the respective modulation frequency ν. Here, ν_P is the intensity modulation frequency of the probe beam (wavelength range: 785 ± 20 nm). We use double modulation at ν_H = 1.3 MHz and ν_P = 1 MHz to reject contributions from 1/*f*-noise. Our setup (see Fig. 1A) enables us to obtain white-light scattering spectra and thus to select NRs with sufficient overlap between LSPR and our probe laser's tuning range. Rotation of polarizer and analyzer orientations in parallel configuration further allows us to determine NR orientation. In the following, we restrict the parameter space by aligning the orientations of incident and analyzed polarization parallel to the NR's long axis and centering of the NR's position in the probe beam's focus. For our measurements, we use NRs with dimensions of 25 × 80 and 40 × 110 nm^2 and typical LSPRs of 1.6 eV (774 nm). For NRs with ≈40 nm diameter, $R_F \gg 1$, and the interference terms in Eq. 1 are negligibly small. In this case, high A_{PT} values are found for probe wavelengths coinciding with the flanks of the NR's LSPR spectrum, i.e., where the slopes of the Lorentzian are highest (see Fig. 1B, left). For the 25- to 20-nm-diameter NRs, $R_F \approx 1$ and high A_{PT} values are found closer to the LSPR's center (see Fig. 1B, center and right). This is expected as $\phi(\nu_P)$ has the highest slopes in proximity to the LSPR frequency and indicates that for NRs with smaller diameters, the $\Delta\phi$ term in Eq. 1 becomes increasingly dominant. Moreover, adjustment of γ via detuning of Δz away from 0 allows us to offset the maxima of the interference terms with respect to ν_{NR} and gives rise to asymmetric spectra (see Fig. 1B, center). To streamline the alignment process, we follow a simple recipe for all NRs: We first center the NR in the focus (*xyz*) by maximizing the scattered intensity with

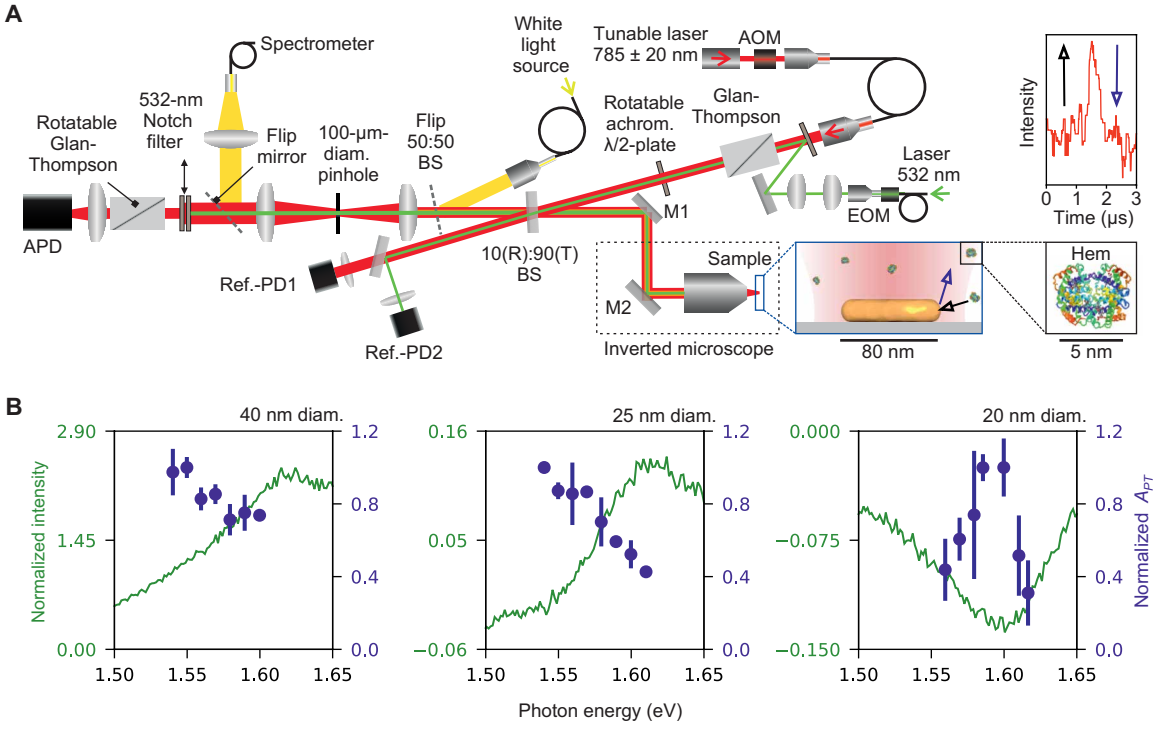

Fig. 1. Experimental setup with photothermal signal optimization. (**A**) The optical setup (left) alongside an illustration of a Hem molecule entering and perturbing an NR's near field (bottom center) and an example of a measured intensity trace showing a short burst caused by such perturbation (top right). Arrows indicate entry and exit of a Hem molecule into and out of the NR's near field and respective changes in detected intensity. (**B**) Sections of white-light scattering spectra normalized to the reflection on the glass slide (green line) and the corresponding relative photothermal amplitude A_{PT} values (blue dots) obtained while varying the tunable laser's wavelength for NRs with various diameters.

crossed polarizers. Then, we optimize A_{PT} with parallel polarizers aligned along the NR's long axis by first tuning the probe wavelength and then adjusting the NR position along the focal axis (z).

Single-molecule measurements

Single-molecule measurements are typically performed by recording intensity time traces of 10 ms length with a sampling rate of 100 MHz using analog avalanche photodiodes working in the linear regime with −3-dB cutoff frequencies of 400 MHz (APD1) and 200 MHz (APD2), whereas in the case of APD1, a low-pass filter with a −3-dB cutoff frequency of 190 MHz was inserted between detector and oscilloscope. These traces are then denoised by applying a running 10-point median filter. Specifically, we detect glucose oxidase (GOx; MW ≈160 kDa) from *Aspergillus niger* (Fig. 2A) (*24*) and Hem (MW ≈64 kDa) from bovine blood (Fig. 2B) (*25*) molecules as they move through the NR's near field. These molecules produce transient shifts of the LSPR, which are recognized as changes of the detected intensity (see Eq. 1). These changes appear on the intensity traces as patterns of two different types: (i) short spike-like perturbations (compare Fig. 2A, I-1, II-1 left, and III-2, and Fig. 2B, II-1, II-2, and III-2), which we interpret as protein molecules moving directly in and out of the near field; and (ii) level-transition patterns (compare Fig. 2A, I-1 and III-1 center, and Fig. 2B, I, III-1, and IV-1), which we attribute to protein molecules moving through the aqueous medium into the near field and then dwelling at the NR's surface owing to attractive forces until the attractive

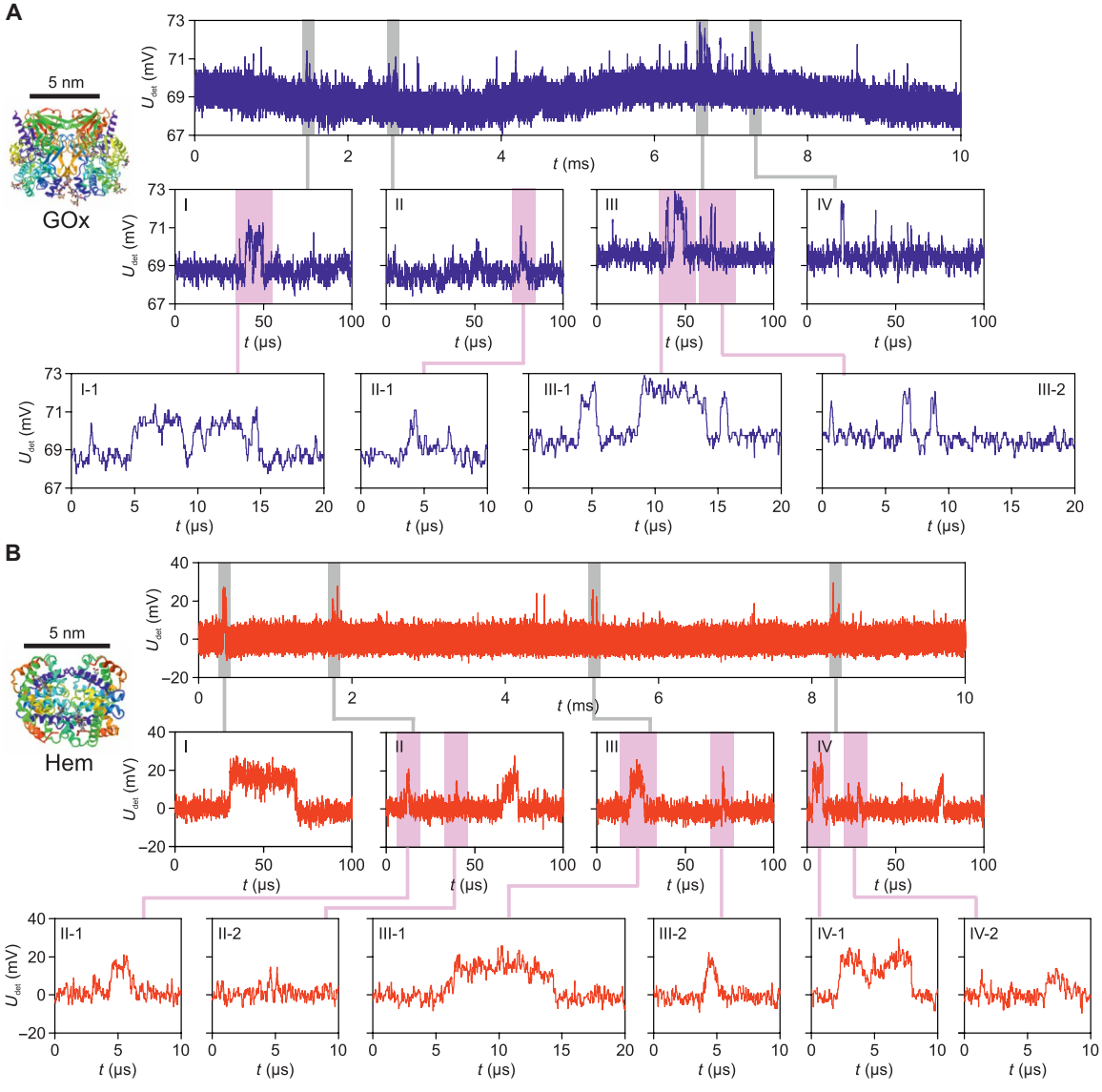

Fig. 2. Transient single-protein detection. Intensity perturbations due to GOx (blue) and Hem (red) molecules moving in an NR's near field. (**A**) Trace (top) and shorter time scale subtraces (I to IV) showing perturbations caused by GOx molecules observed with a 25-nm-diameter NR and a DC-coupled detector. (**B**) Trace (top) and shorter time scale subtraces (I to IV) showing perturbations caused by Hem molecules observed with a 40-nm-diameter NR and an AC-coupled detector. Most perturbations exhibit sub-microsecond rise and fall times. Longer perturbations as shown in (A), I-1 and III-1 center, and (B), I, III-1, and IV-1, are likely caused by attractive interactions between analyte and NR. All traces were recorded with Δt = 10 ns and denoised with a 10-point median filter. Protein concentrations were 500 nM (A, GOx) and 30 nM (B, Hem).

potential is eventually overcome and they again move out of the near field. We also observed a few binding and unbinding events without their respective counterparts in the same trace. This means that sticking lasting longer than the trace length of 10 ms can occur. To obtain statistics, we count fluctuations on intensity traces as events if their amplitudes exceed 5σ, where σ is the SD of the whole trace. This does not include rare single-step events without counterpart in the same trace (GOx). GOx measurements were performed using the DC-coupled APD1. For the Hem measurements shown in Figs. 2, 3, and 4, APD2 was used. APD2 is AC-coupled and, because of its low-frequency cutoff (1.5 kHz), can introduce artificially decaying amplitudes on longer events. To avoid contributions from these artifacts, events with durations longer than 0.1 ms were excluded from analysis.

For each event, we determine the maximum amplitudes ΔI_{max} and the following temporal properties: τ_{rise} (τ_{fall}), the rise (fall) time, i.e., the time it takes from the beginning (end) of the event to rise (fall) to (from) half the maximum, and the duration between these points, i.e., the full duration at half maximum (FDHM). For both Hem and GOx, we find rise and fall times in the range from 10 to 1000 ns (see Fig. 3, A and B). All τ_{rise} and τ_{fall} distributions fit well to mono-exponential decays [i.e., to $f(t) = N\frac{t}{\tau}e^{-t/\tau}$ for the logarithmically spaced distributions] and we find rise (fall) decay times of 101 ± 8 ns (108 ± 6 ns) for GOx and 153 ± 11 ns (155 ± 11 ns) for Hem. The similarity between rise- and fall-time distributions suggests that entry and the exit processes of both proteins into and out of the NR's sensitive volume are subject to equivalent interactions. The two-dimensional (2D) histograms (Fig. 3, A and B, center) further

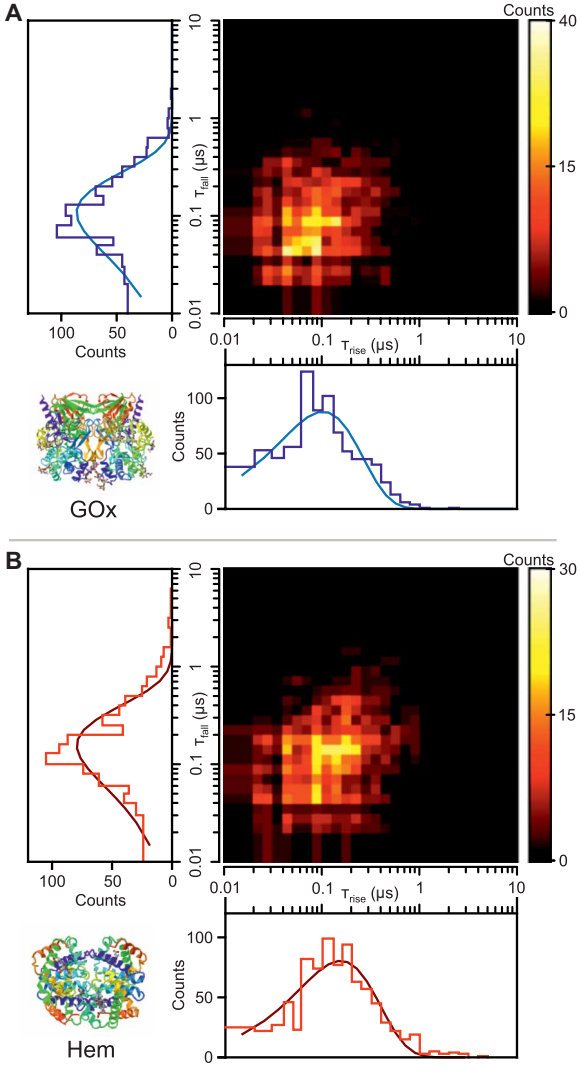

Fig. 3. Rise and fall time distributions of single-protein detection events. Statistics of rise and fall times, characterizing the molecular diffusion in the absence of sticking and immediately before and after sticking, for GOx (**A**) and Hem (**B**). Each panel (A and B) shows the τ_{rise} (bottom) and τ_{fall} (right) distributions alongside their respective two-dimensional (2D) histograms (center). Solid lines (A, light blue and B, dark red) in the distributions show fits to mono-exponential time distributions plotted on logarithmic scale of times.

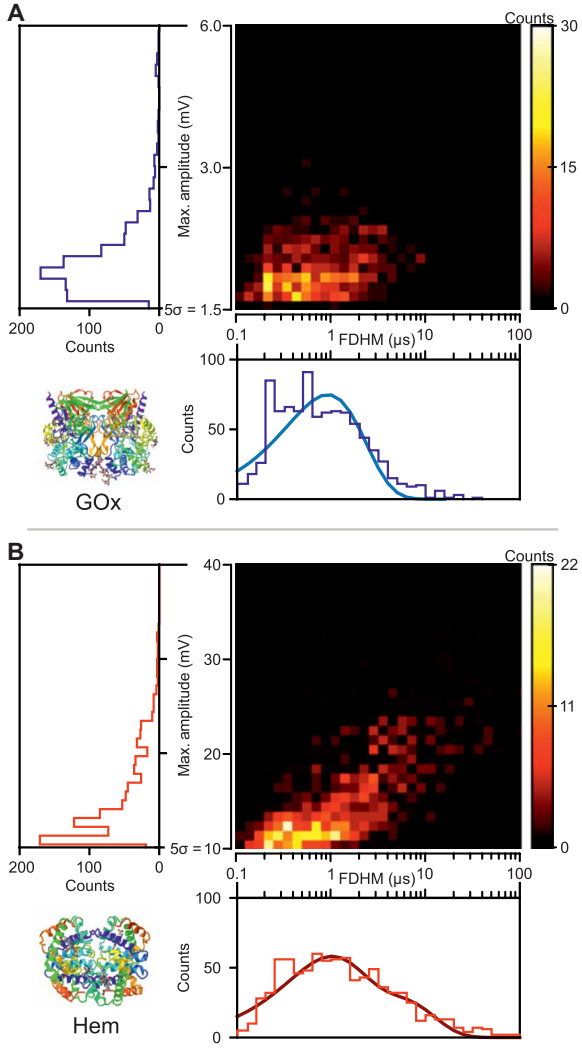

Fig. 4. Dwell time and amplitude distributions of single-protein detection events. Statistics of dwell times and amplitudes as obtained for GOx (**A**) and Hem (**B**). Each panel (A and B) shows the full duration at half maximum (FDHM) (bottom) and maximum amplitude (right) distributions alongside their respective 2D histograms (center). Solid lines in the FDHM distributions show fits to mono-exponential (A, light blue) and bi-exponential time distributions, plotted on logarithmic scale of times (B, dark red).

exhibit no apparent correlation between τ_{rise} and τ_{fall} for individual events. This missing correlation shows that entry and exit processes into and out of near field are mutually independent as expected for Brownian motion. The rise and fall times for GOx are shorter than the ones we find for Hem although GOx exhibits the higher molecular weight. We attribute this difference to two factors: (i) The difference between the near-field extents due to the different dimensions of the NRs used for these measurements (see fig. S4, Systems I and III). GOx was observed with the smaller NR and thus we expect shorter rise and fall times. (ii) Contributions due to rotational diffusion of the more anisotropic GOx (in comparison to the globular Hem). We find distinctive differences between the intensity autocorrelation curves of both molecules. Specifically, we observe a continued increase in correlation toward shorter times on the sub–100-ns scale for GOx, which is absent for Hem (see fig. S1). This time scale agrees well with the estimated rotational diffusion time of GOx, on the order of 50 ns, and lies within our temporal resolution (see section S1). Rotational and translation diffusion are coupled and, for our system, exhibit similar characteristic times in the 10- to 100-ns range. Thus, a clear distinction between contributions by both processes on a single-event basis is challenging and further work beyond the scope of this manuscript is needed to confirm the observation of rotational diffusion. We now want to discuss the FDHM distributions found for both protein species. These times represent the dwell time of individual proteins in the NR's sensitive volume. They are centered around ≈1 μs and distributed over ranges from 100 ns up to few tens of microseconds, i.e., substantially longer than the rise and fall times alone (see Fig. 3B). Here, the stretch toward long time scales is likely due to attractive interactions between the proteins and the NR's surface and indicates unspecific sticking. The FDHM distribution of Hem (Fig. 4B, bottom) is more stretched toward long times than the one of GOx (Fig. 4A, bottom). Specifically, we find that the FDHM distribution for GOx fits well to a monoexponential decay as expected for a Langmuir adsorption process governed by a single time constant for which we find $\tau = 0.9$ μs from the respective fit. For Hem, this is not the case, as the single-rate fit clearly deviates from the data (not shown). This suggests contributions from multiple processes with different rates. Already for two rates ($\tau_1 = 0.83$ μs and $\tau_2 = 4.8$ μs), we find a much better match. This is rather expected because of the larger set of fitting parameters. We, however, think that a broader spectrum of rates exists rather than just two. The maximum amplitude versus FDHM distribution for Hem (Fig. 4B, center) also reveals a stronger correlation between larger amplitudes and longer times as compared with GOx (Fig. 4A, center). We think that the differences between Hem and GOx, specifically the existence of multiple rate constants is due to one of the following reasons: (i) Hem exhibits surface areas that have different affinity to gold and therefore Hem shows different sticking dynamics dependent on the protein's contact area with the surface. In this case, the correlation of high amplitudes with long FDHMs arises because of increased overlap between protein sections with high polarizability (i.e., Hem's iron complex) and the NR's near field. (ii) Hem has different affinities to different types of gold crystal facets. In this case, the correlation of higher maximum amplitudes with longer FDHMs implies that facets that offer higher affinities coincide with zones of higher near-field intensity. Which hypothesis is right or whether there is a process we have not covered will require further study beyond the scope of this work.

Proof of single-protein detection

In the following, we will provide evidence based on multiple aspects of our data and complementary measurements, which, together, provide strong evidence that the observed events indeed arise form perturbation caused by single-protein molecules.

1) Time scales of event dynamics: For both GOx and Hem, we observed rise and fall times on the order of 105 and 155 ns, respectively. To evaluate the distance dependence of the observed amplitudes, we have performed boundary element method (BEM) (*26*) simulations of our NR-protein systems. From those simulations, we find decay lengths of $d_{L,\,Hem} = 8.4$ nm and $d_{L,\,Gox} = 4.8$ nm for the respective systems (see section S3, Systems I and III, and fig. S4). Using these values as rms displacements and the rise and fall times as diffusion time, we can determine the hydrodynamic radius of our analytes via the Stokes-Einstein relation

$$r_H = \frac{k_b T \tau_{\mathrm{fall}}}{\pi \eta d_{half}^2} \tag{2}$$

where k_b is Boltzmann's constant, T is the temperature, and η is the viscosity of water. We find $r_H = 2.8 \pm 0.6$ nm for Hem, which is an excellent match with the literature value of 3.11 nm (*27*, *28*) and agrees well with the value of 3.9 ± 1.1 nm determined via dynamic light scattering (DLS; see fig. S7). For GOx, we find $r_H = 5.8 \pm 1.3$, a value that within the error comes close to the literature values of 4.45 nm (*29*) and 5.7 nm (*30*) and agrees well with the value of 5.3 ± 1.3 nm determined via DLS (see fig. S8).

2) Amplitude of detected events: Here, we first have to point out that GOx and Hem measurements shown in Figs. 2, 3, and 4 were performed with different detectors; i.e., the amplitude values given are not directly comparable. To obtain a direct comparison of perturbation amplitudes, we determine the relative intensity changes $\Delta I_{\mathrm{rel}} = |\frac{\Delta I_{\max}}{I_{det}}|$ caused by GOx and Hem from measurements performed with the same DC-coupled detector and NRs of similar dimensions. We find average values of $\overline{\Delta I_{rel}} = (3.4 \pm 1.5)\,\%$ for GOx and (1.55 ± 0.45)% for Hem. From BEM simulations of our NR-protein systems (section S3, Systems II and III, and fig. S4), we find maximum relative changes in the scattering cross sections with values of $\Delta\sigma_{Hem} = 0.8\%$ and $\Delta\sigma_{GOx} = 1.74\%$. These values are a factor ≈2 lower than the experimental values. This discrepancy is a direct result of our measurement methodology, i.e., the use of interference scattering. For the NRs used here, we experimentally determined values of $R_F^2 = 1.7$ (Hem) and $R_F^2 = 1.8$ (GOx). From these values and our BEM simulation results, we determine upper bounds for the ΔI_{rel} values achievable via our interference-based method (see section S3). We find $\Delta I_{rel,\,max} = 1.9\%$ for Hem (see fig. S5A) and $\Delta I_{rel,\,max} = 3.5\%$ for GOx (see fig. S5B). These values are 2.4- and 2-fold higher than the ones achievable by pure scattering-based methods and agree well with our experimental results. Moreover, also the ratio $\Delta I_{GOx}/\Delta I_{Hem} = 1.84$ is in good agreement with the experimental value of $\overline{\Delta I_{rel}}(\mathrm{GOx})\,/\,\overline{\Delta I_{rel}}(\mathrm{Hem}) = 2.2 \pm 1$. In the case of GOx, some of the experimental ΔI_{rel} values exceed the upper bound. We attribute this discrepancy to the fact that we simulated both proteins as spheres. We believe that this simple model results in an underestimation of the intensity changes caused by GOx, which deviates more from a spherical shape than Hem. Zijlstra *et al.* (*7*) had observed a similar discrepancy between simulations on the basis of spherical models and their experimental results, which yielded LSPR shifts ≈2 times higher than expected.

3) Statistical evidence: We have performed measurements at different analyte concentrations and find a linear dependence between event rate and analyte concentration (section S4 and fig. S6A). We also find that the inter-event times follow a Poissonian distribution (see section S4 and fig. S6B). Both findings together prove that events are mutually independent and are caused neither by multiple simultaneous entry of multiple proteins into the near field nor by the formation of aggregates, processes for which a nonlinear scaling between rate and concentration is expected. In addition, we did not detect events in the absence of analytes. Thus, the presence of impurities with non-negligible concentrations in the used supernatants can be ruled out. We further do not recognize protein aggregates in our DLS measurements (see section S5). Together, these three arguments provide convincing evidence that we indeed detect single proteins.

Detection limits

In the following, we discuss the detection limits of our system. Since the production of APD2 has been discontinued, we will restrict this analysis to measurements performed with APD1. From our postprocessed data, we determine SNRs of up to ≈15 for GOx at an incident power of 0.81 mW. Thus, a ≈10-kDa protein could, in principle, be detected at an SNR of 1 with the same configuration. Our postprocessing method involved a median filter that exhibits nonlinear filtering characteristics; thus, we continue the discussion on the basis of raw unfiltered data for which we find an SNR of 2.7 (GOx) yielding a mass detection limit of $m_{LOD} = 8.4\ \mathrm{Da(Hz)}^{-1/2}$. From calibration measurements, we determined an excess noise factor of 1.7 and an NEP of 0.6 pW $(\mathrm{Hz})^{-1/2}$ for the used detector setting. In a shot noise–limited setting, i.e., in the absence of electronic and excess noise, we estimate that an SNR of 5.9 (GOx), i.e., $m_{LOD} = 3.8\ \mathrm{Da}\ (\mathrm{Hz})^{-1/2}$ is achievable under the same experimental circumstances. Using postprocessing, i.e., 10-point median filtering, shot noise–limited detection would then push the SNR toward ≈32 for GOx, i.e., enable the detection of 5-kDa proteins at an SNR of 1.

DISCUSSION

To begin the discussion, we would first like to put our time resolution into context: None of the events discussed above, even the longest one (FDHM ≈100 μs), would be resolved with other state-of-the-art nanoplasmonic assays (*6*–*14*, *31*–*33*), which typically exhibit time resolutions in the order of milliseconds; i.e., they would see the whole extent of the traces displayed in Fig. 2A (top) and Fig. 2B (top) as either a single or a set of few points. We think that being able to resolve and analyze such short unspecific interactions opens up a whole new pathway for fast molecular fingerprinting. We envision that previously hidden differences in the interaction dynamics between specific protein subdomains and small weakly bonding receptor molecules on the NR's surface may be used as means to distinguish between proteins of similar mass. In the simplest case, the average number of formed bonds determines the dwell time. This would further allow us to gain structural information on analytes, especially unknown ones, therefore mitigating the need for target-specific receptors. In addition, physical analyte properties such as Stokes radius and molecular weight may be determined via τ_{rise}, τ_{fall}, and relative amplitudes following NR calibration with a suited standard. We further envision that in combination with purpose-tailored plasmonic structures, which will improve on the relatively modest enhancement and confinement of NR near fields, our method will be able to resolve fast changes in the structure and shape of single proteins purposely positioned inside their near fields.

In conclusion, we have demonstrated the transient detection of single proteins with masses as low as 64 kDa traversing the subattoliter volumes spanned by plasmonic near fields during times as short as 100 ns and with an SNR exceeding 5. We have used our unprecedented temporal resolution to observe protein motion. From our experiments, we determined hydrodynamic radii that agree well with literature values and with complementary DLS measurements. Moreover, relative signal amplitudes scale as expected and agree with simulation results. We further found initial evidence that suggests that our method may resolve rotational diffusion and thus provide information on protein anisotropy. This shows that our method can simultaneously probe Stokes radius and polarizability of a protein and demonstrates its potential for future high-throughput fingerprinting applications. By observing the dynamics of unspecific protein-surface interactions, we also found distinctive differences in sticking behaviors of GOx and Hem. We think that this result offers but a glimpse of the additional information that may be gained on physical and biochemical processes, now made accessible by fast optoplasmonic detection.

MATERIALS AND METHODS

Optical setup

Here, we list the components used in our measurements:

Objective: Olympus UPLFLN100XOP
Tube lens: Olympus Super Wide Tube Lens Unit
Lasers: Toptica DL pro 785 nm and Cobolt Samba 532 nm
APD1: Thorlabs APD430A/M (DC-Coupled)
APD2: Helix-902-200 (Excelitas Technologies) (AC-Coupled)
10:90 Beamsplitter BSN11 (Thorlabs)
Glan-Thompson Polarizer GTH10M-B (Thorlabs)
Piezo Translator P-561.3CD (Physik Instrumente GmbH & Co KG)
White-light source: EQ-99XFC (Energetiq)
Spectrometer: QE-65000 (Ocean Optics)
Reference Photodiodes 1 and 2: PDA36A2 (Thorlabs) and HCA-S-200M (Femto)
EOM: Amplitude Modulator AM532 (Jenoptik)
AOM: MT110-A1-IR (AA Opto-Electronic)
Achromatic λ/2-plate: RAC 4.2.10 (B. Halle)
Notch Filter: ZET532NF (Chroma)

Photodetection and data acquisition

In contrast to single-photon counting APDs, the APDs we use are linear; i.e., they provide an intensity-proportional output current that is then converted into a voltage via a trans-impedance amplifier and, thus, they have no dead time. In this regard, they operate similarly to normal photodiodes; however, their photocurrent is already amplified inside the diode itself via the avalanche effect. This unfortunately gives rise to additional statistical noise—called excess noise. Because of this excess noise, these detectors cannot operate at the shot noise limit. In comparison to normal photodiodes, however, they have substantially better (lower) NEP—i.e., they overcome the electronic noise floor at lower intensities. This is essential for our measurements as our signal would otherwise vanish

in the electronic noise floor of normal PIN photodiodes (which can work at the shot noise limit).

Our detectors have a −3-dB bandwidth of 400 MHz (APD1) and 200 MHz (APD2), respectively. We sample our data with a rate of 10^8 samples/s (Oscilloscope: WaveSurfer 24MXs-B, Teledyne Lecroy). We use a low-pass filter with a −3-dB cutoff frequency of 190 MHz between the 400 MHz and the recording oscilloscope (this is to reject noise from higher frequencies in excess of the sampling rate). The response times of both detectors and the connected electronics are thus 5.3 and 5 ns, respectively. This is faster than our sampling rate and substantially faster than the average rise and fall times of the observed events. In consequence, we can safely exclude electronic artifacts due to electronic response times on our signals.

Slide preparation

Cetyltrimethylammonium bromide (CTAB)-capped gold NRs were purchased from Nanopartz. GNR stock solutions containing 10 mM CTAB were sonicated (20 min; Branson 2510) and then deposited onto glass slides (Borosilicate glass diameter 25-mm thickness No. 1, VWR), which were previously sonicated in ethanol and Milli-Q (30 min; each Branson 2510), via spin-coating (Specialty Coating Systems Spin Coater 6700). The CTAB layer was consequently removed via ultraviolet cleaning (10 to 60 min; Ossila), and the slide was rinsed with Milli-Q water.

Protein measurements

Solutions containing various concentrations of Hem and GOx were freshly prepared before the start of each measurement. For GOx, we used aqueous solutions (Milli-Q water) containing 20 mM sodium chloride, and for Hem, we used 1× phosphate-buffered saline buffer solutions. All chemicals and proteins were purchased from Sigma-Aldrich.

SUPPLEMENTARY MATERIALS

Supplementary material for this article is available at https://science.org/doi/10.1126/sciadv.abl5576

REFERENCES AND NOTES

1. H. Y. Aviram, M. Pirchi, H. Mazal, Y. Barak, I. Riven, G. Haran, Direct observation of ultrafast large-scale dynamics of an enzyme under turnover conditions. *Proc. Natl. Acad. Sci. U.S.A.* **115**, 3243–3248 (2018).
2. R. M. Ballew, J. Sabelko, M. Gruebele, Direct observation of fast protein folding: The initial collapse of apomyoglobin. *Proc. Natl. Acad. Sci. U.S.A.* **93**, 5759–5764 (1996).
3. J. Kubelka, J. Hofrichter, W. A. Eaton, The protein folding 'speed limit'. *Curr. Opin. Struct. Biol.* **14**, 76–88 (2004).
4. D. Nettels, I. V. Gopich, A. Hoffmann, B. Schuler, Ultrafast dynamics of protein collapse from single-molecule photon statistics. *Proc. Natl. Acad. Sci. U.S.A.* **104**, 2655–2660 (2007).
5. H. Mazal, G. Haran, Single-molecule FRET methods to study the dynamics of proteins at work. *Curr. Opin. Biomed. Eng.* **12**, 8–17 (2019).
6. I. Ament, J. Prasad, A. Henkel, S. Schmachtel, C. Sönnichsen, Single unlabeled protein detection on individual plasmonic nanoparticles. *Nano Lett.* **12**, 1092–1095 (2012).
7. P. Zijlstra, P. M. R. Paulo, M. Orrit, Optical detection of single non-absorbing molecules using the surface plasmon resonance of a gold nanorod. *Nat. Nanotechnol.* **7**, 379–382 (2012).
8. V. R. Dantham, S. Holler, C. Barbre, D. Keng, V. Kolchenko, S. Arnold, Label-free detection of single protein using a nanoplasmonic-photonic hybrid microcavity. *Nano Lett.* **13**, 3347–3351 (2013).
9. C. Rosman, J. Prasad, A. Neiser, A. Henkel, J. Edgar, C. Sönnichsen, Multiplexed plasmon sensor for rapid label-free analyte detection. *Nano Lett.* **13**, 3243–3247 (2013).
10. M. D. Baaske, M. R. Foreman, F. Vollmer, Single-molecule nucleic acid interactions monitored on a label-free microcavity biosensor platform. *Nat. Nanotechnol.* **9**, 933–939 (2014).
11. M. A. Beuwer, M. W. J. Prins, P. Zijlstra, Stochastic protein interactions monitored by hundreds of single-molecule plasmonic biosensors. *Nano Lett.* **15**, 3507–3511 (2015).
12. M. D. Baaske, F. Vollmer, Optical observation of single atomic ions interacting with plasmonic nanorods in aqueous solution. *Nat. Photonics* **10**, 733–739 (2016).
13. E. Kim, M. D. Baaske, F. Vollmer, In situ observation of single-molecule surface reactions from low to high affinities. *Adv. Mater.* **28**, 9941–9948 (2016).
14. P. Zhang, G. Ma, W. Dong, Z. Wan, S. Wang, N. Tao, Plasmonic scattering imaging of single proteins and binding kinetics. *Nat. Methods* **17**, 1010–1017 (2020).
15. M. D. Baaske, P. S. Neu, M. Orrit, Label-free plasmonic detection of untethered nanometer-sized brownian particles. *ACS Nano* **14**, 14212–14218 (2020).
16. M. Piliarik, V. Sandoghdar, Direct optical sensing of single unlabelled proteins and super-resolution imaging of their binding sites. *Nat. Commun.* **5**, 4495 (2014).
17. G. Young, N. Hundt, D. Cole, A. Fineberg, J. Andrecka, A. Tyler, A. Olerinyova, A. Ansari, E. G. Marklund, M. P. Collier, S. A. Chandler, O. Tkachenko, J. Allen, M. Crispin, N. Billington, Y. Takagi, J. R. Sellers, C. Eichmann, P. Selenko, L. Frey, R. Riek, M. R. Galpin, W. B. Struwe, J. L. P. Benesch, P. Kukura, Quantitative mass imaging of single biological macromolecules. *Science* **360**, 423–427 (2018).
18. M. Liebel, J. T. Hugall, N. F. Van Hulst, Ultrasensitive label-free nanosensing and high-speed tracking of single proteins. *Nano Lett.* **17**, 1277–1281 (2017).
19. D. Cole, G. Young, A. Weigel, A. Sebesta, P. Kukura, Label-free single-molecule imaging with numerical-aperture-shaped interferometric scattering microscopy. *ACS Photonics* **4**, 211–216 (2017).
20. A. Gaiduk, M. Yorulmaz, P. V. Ruijgrok, M. Orrit, Room-temperature detection of a single molecule's absorption by photothermal contrast. *Science* **330**, 353–356 (2010).
21. M. Selmke, M. Braun, F. Cichos, Photothermal single-particle microscopy: Detection of a nanolens. *ACS Nano* **6**, 2741–2749 (2012).
22. S. Adhikari, P. Spaeth, A. Kar, M. D. Baaske, S. Khatua, M. Orrit, Photothermal microscopy: Imaging the optical absorption of single nanoparticles and single molecules. *ACS Nano* **14**, 16414–16445 (2020).
23. C. Chen, H. Shimizu, T. Kitamori, Review of ultrasensitive readout for micro–/nanofluidic devices by thermal lens microscopy. *J. Opt. Microsystems.* **1**, 035001–035007 (2021).
24. G. Wohlfahrt, S. Witt, J. Hendle, D. Schomburg, H. M. Kalisz, H.-J. Hecht, 1.8 and 1.9 Å resolution structures of the *Penicillium amagasakiense* and *Aspergillus niger* glucose oxidases as a basis for modelling substrate complexes. *Acta Crystallogr. D* **55**, 969–977 (1999).
25. R. Aranda, H. Cai, C. E. Worley, E. J. Levin, R. Li, J. S. Olson, G. N. Phillips Jr., M. P. Richards, Structural analysis of fish versus mammalian hemoglobins: Effect of the heme pocket environment on autooxidation and hemin loss. *Proteins* **75**, 217–230 (2009).
26. U. Hohenester, A. Trügler, MNPBEM—A Matlab toolbox for the simulation of plasmonic nanoparticles. *Comput. Phys. Commun.* **183**, 370–381 (2012).
27. S. Beretta, G. Chirico, D. Arosio, G. Baldini, Photon correlation spectroscopy of interacting and dissociating hemoglobin. *J. Chem. Phys.* **106**, 8427–8435 (1997).
28. D. Arosio, H. E. Kwansa, H. Gering, G. Piszczek, E. Bucci, Static and dynamic light scattering approach to the hydration of hemoglobin and its supertetramers in the presence of osmolites. *Biopolymers* **63**, 1–11 (2002).
29. O. Courjean, F. Gao, N. Mano, Deglycosylation of glucose oxidase for direct and efficient glucose electrooxidation on a glassy carbon electrode. *Angew. Chem. Int. Ed. Engl.* **48**, 5897–5899 (2009).
30. D. W. Ritter, J. R. Roberts, M. J. McShane, Glycosylation site-targeted PEGylation of glucose oxidase retains native enzymatic activity. *Enzyme Microb. Technol.* **52**, 279–285 (2013).
31. E. Kim, M. D. Baaske, I. Schuldes, P. S. Wilsch, F. Vollmer, Label-free optical detection of single enzyme-reactant reactions and associated conformational changes. *Sci. Adv.* **3**, e1603044 (2017).
32. S. Subramanian, H. B. L. Jones, S. Frustaci, S. Winter, M. W. van der Kamp, V. L. Arcus, C. R. Pudney, F. Vollmer, Sensing enzyme activation heat capacity at the single-molecule level using gold-nanorod-based optical whispering gallery modes. *ACS Appl. Nano Mater.* **4**, 4576–4583 (2021).
33. V. Wulf, F. Knoch, T. Speck, C. Sönnichsen, Gold nanorods as plasmonic sensors for particle diffusion. *J. Phys. Chem. Lett.* **7**, 4951–4955 (2016).

Acknowledgments

Funding: This work was supported by the Netherlands Organisation for Scientific Research (NWO) and has received funding from the European Union's Horizon 2020 research and innovation programme under the Marie Skłodowska-Curie Grant Agreement no. 792595 (MDB). **Author contributions:** M.D.B. and M.O. conceived the idea. M.D.B. planned the experiments and performed BEM simulations. M.D.B. and N.A. built the optical setup. M.D.B. performed experiments and data analysis. N.A. performed DLS measurements. D.P. obtained and analyzed SEM micrographs. M.D.B. and M.O. wrote the manuscript. All authors commented on the manuscript. **Competing interests:** The authors declare that they have no competing interests. **Data and materials availability:** All data needed to evaluate the conclusions in the paper are present in the paper and/or the Supplementary Materials.

Submitted 21 July 2021
Accepted 22 November 2021
Published 14 January 2022
10.1126/sciadv.abl5576

ScienceAdvances

Nanosecond time scale transient optoplasmonic detection of single proteins

Martin D. Baaske, Nasrin Asgari, Deep Punj, and Michel Orrit

Sci. Adv., **8** (2), eabl5576.
DOI: 10.1126/sciadv.abl5576

Science Advances (ISSN) is published by the American Association for the Advancement of Science. 1200 New York Avenue NW, Washington, DC 20005. The title *Science Advances* is a registered trademark of AAAS.